Experimental Eye Research 172 (2018) 86–93

Contents lists available at ScienceDirect

Experimental Eye Research

journal homepage: www.elsevier.com/locate/yexer

Effect of a contact lens on mouse retinal *in vivo* imaging: Effective focal length changes and monochromatic aberrations

Pengfei Zhang[a], Jacopo Mocci[b], Daniel J. Wahl[c], Ratheesh Kumar Meleppat[a], Suman K. Manna[a], Martino Quintavalla[b], Riccardo Muradore[d], Marinko V. Sarunic[c], Stefano Bonora[b], Edward N. Pugh Jr.[a,e], Robert J. Zawadzki[a,e,*]

[a] UC Davis Eye-Pod Small Animal Ocular Imaging Laboratory, Department of Cell Biology and Human Anatomy, University of California Davis, 4320 Tupper Hall, Davis, CA 95616, United States
[b] CNR-Institute for Photonics and Nanotechnology, Via Trasea 7, 35131, Padova, Italy
[c] Engineering Science, Simon Fraser University, Burnaby BC, V5A 1S6, Canada
[d] Department of Computer Science, University of Verona, Italy
[e] UC Davis Eye Center, Dept. of Ophthalmology & Vision Science, University of California Davis, 4860 Y Street, Suite 2400, Sacramento, CA 95817, United States

ARTICLE INFO

Keywords:
Contact lens
Effective focal length
Mouse eye aberration
Adaptive optics
Scanning laser ophthalmoscope

ABSTRACT

For *in vivo* mouse retinal imaging, especially with Adaptive Optics instruments, application of a contact lens is desirable, as it allows maintenance of cornea hydration and helps to prevent cataract formation during lengthy imaging sessions. However, since the refractive elements of the eye (cornea and lens) serve as the objective for most *in vivo* retinal imaging systems, the use of a contact lens, even with 0 Dpt. refractive power, can alter the system's optical properties. In this investigation we examined the effective focal length change and the aberrations that arise from use of a contact lens. First, focal length changes were simulated with a Zemax mouse eye model. Then ocular aberrations with and without a 0 Dpt. contact lens were measured with a Shack-Hartmann wavefront sensor (SHWS) in a customized AO-SLO system. Total RMS wavefront errors were measured for two groups of mice (14-month, and 2.5-month-old), decomposed into 66 Zernike aberration terms, and compared. These data revealed that vertical coma and spherical aberrations were increased with use of a contact lens in our system. Based on the ocular wavefront data we evaluated the effect of the contact lens on the imaging system performance as a function of the pupil size. Both RMS error and Strehl ratios were quantified for the two groups of mice, with and without contact lenses, and for different input beam sizes. These results provide information for determining optimum pupil size for retinal imaging without adaptive optics, and raise critical issues for design of mouse optical imaging systems that incorporate contact lenses.

1. Introduction

The mouse is an important model organism in biomedical research, and offers many models of eye diseases used in basic and applied ophthalmology and vision science research (Zhang et al, 2017; Helmstaedter et al, 2013; Jiang et al, 1996; Fuerst et al, 2008). Historically most mouse retinal imaging studies have been performed *ex vivo* with histology and confocal microscopy. More recently *in vivo* retinal imaging methods, including Scanning Laser Ophthalmoscopy (SLO) (Webb and Hughes, 1981; Seeliger et al, 2005; Paques et al, 2006; Clemens et al., 2012), Optical Coherence Tomography (OCT) (Huang et al, 1991; Srinivasan et al, 2006; Fischer et al, 2009) and their combination (Zhang et al, 2015a), with or without Adaptive Optics (AO) (Geng et al, 2012; Biss et al, 2007; Guevara-Torres et al., 2015; Zawadzki et al, 2015), have been used. All these *in vivo* imaging techniques use the mouse eye's optics as the imaging objective. The numerical aperture (NA) of the mouse eye is more than twice that of the human eye, and thus potentially offers at least two-fold better lateral and four-fold better axial resolution (Geng et al, 2011).

Unlike humans, mice are usually anesthetized during retinal imaging. This typical experimental condition inhibits mouse eye blinking and results in corneal drying over time. So, unless contravening steps are taken, the cornea becomes optically cloudy (Bermudez et al, 2011). One solution to this problem is to frequently apply artificial tears to maintain a moist cornea. However, this interrupts imaging. Moreover, the residual uneven tear film on the cornea can distort the eye's front

* Corresponding author. UC Davis Eye-Pod Small Animal Ocular Imaging Laboratory, Department of Cell Biology and Human Anatomy, University of California Davis, 4320 Tupper Hall, Davis, CA 95616, United States.
E-mail address: rjzawadzki@ucdavis.edu (R.J. Zawadzki).

https://doi.org/10.1016/j.exer.2018.03.027
Received 13 December 2017; Received in revised form 26 February 2018; Accepted 27 March 2018
Available online 28 March 2018

surface and introduce undesirable aberrations, especially in AO systems, which work over larger pupil sizes. Certainly, continuous imaging without any interruption is desired to obtain high-quality images for structural and functional analysis of the retina.

Specialized contact lenses with additional gel are often used to maintain corneal wetness and prevent cataract formation in mice (Zhang et al, 2015a; Geng et al, 2012; Zawadzki et al, 2015; Liu et al, 2013). The contact lens is situated at the cornea or close to it, and serves as the initial refractive element of the compound objective. Consequently, the contact lens and gel alter the optical properties of the "objective", including its effective focal length and aberrations. There are two possible ways of using a contact lens in mouse ocular imaging: in one approach the contact lens is placed directly on the mouse eye; in the second the contact lens is attached rigidly to the system optics. In first case the experimenter has no direct control over the contact lens position or the thickness of the gel between the cornea and contact lens. In the second, as described in this study, the experimenter can manipulate the distance and relative position between the cornea and contact lens to a certain degree. One potential way to determine to the effect of a contact lens on the mouse eye's optics is to characterize wavefront aberrations with and without the contact lens in different mouse populations, as done in humans (Thibos et al, 2002; Porter et al, 2001; Castejón-Mochón et al, 2002).

In this report we first simulate the effect of a contact lens in terms of the effective focal length of the mouse model eye using Zemax. Next, we present the empirical results of its effect on ocular aberrations for two groups of C57BL/6J (pigmented) mice: 2.5-month-old (n = 10 eyes) and 14-month-old (n = 10 eyes). Ocular aberrations measured with and without contact lenses with a custom mouse retinal AO-SLO system employed with Shack-Hartmann wavefront sensor (Zawadzki et al, 2015) are presented. The major aberrations introduced by use of a contact lens are identified, and the aberration statistics for the two groups are compared as a function of pupil size. Finally, we present the equivalent lateral resolution and Strehl ratio for different imaging beam sizes at the mouse pupil.

2. Methods

We used a custom AO-SLO imaging system (Zawadzki et al, 2015) to measure mouse eye aberrations. As shown in Fig. 1, the system employs a cascade of afocal telescopes, created by pairs of spherical mirrors (Lambda Research Optics Inc., Costa Mesa, California, US) and one achromatic lens (Ross Optical, EI Paso, Texas, US) to optically relay eye pupil to all key optical components, including: the horizontal- and vertical-scanning mirrors, the wavefront corrector (deformable mirror (DM), DM97-15, AlpAO, France) and the Shack-Hartmann wavefront sensor (SHWS). The system uses light from a superluminescent diode (663 nm center wavelength, 10 nm bandwidth, Superlum, SLD-26-HP) for both wavefront sensing and reflectance imaging. At the mouse pupil plane, the beam size is 2 mm in diameter by design, as defined by the aperture size of the DM. The SHWS in our AO-SLO system was recently upgraded and placed on axis with the exit pupil to ensure minimal distortion in the measured wavefront.

The left inset of Fig. 1 shows a photo of the SHWS (Photon Loop, Dynamic Optics srl, Padova, Italy (Mocci et al., 2018)), which consists of a lenslet array (Pitch = 150 µm, calibrated f = 6.43 mm, MLA150-5C-M, Thorlabs) and a CMOS camera (UI306xcp-M; IDS Imaging Development Systems GmbH). The camera pixel size is 5.86 µm, thus each lenslet is covered by 25 × 25 pixels on the camera. The right inset shows both the design drawing and the photo of the prototype mount for the contact lens. The mount allows imaging with a field-of-view (FOV) of 56° and a 2.5 mm aperture at the pupil position. The replaceable contact lens is fixed to the mount by general purpose adhesive.

In these experiments the same beam served for imaging and wavefront sensing, and had a power at the mouse pupil of 100 µW. The scanning FOV was fixed at 0.88° visual angle during measurment of the wavefront aberrations to stay within isoplanatic angle. The scanning and image data acquisition (1102039 B.C. LTD, Burnaby, British Columbia Canada) with 400 × 200 pixels resolution was run at 10 Hz frame rate. The pupil at the mouse eye (2 mm) was magnified 3-fold at the conjugate plane of the SHWS (6 mm). The pupil at the SHWS defines a circular aperture with a diameter of 40 lenslets, and a total of 1264 active lenslets (green dots shown in Fig. 2 (a)) were used for wavefront sampling. The wavefront sensor system was run at 100 Hz, limited by the exposure time and the wavefront reconstruction computation time. Before measuring the mouse eye aberrations, the system residual aberrations were removed using an artificial eye model with a 100-mm focal length achromatic doublet (AC254-100-A, Thorlabs, US), and white copy machine paper at its focus. The residual system aberration and its corresponding simulated fringle map before (Fig. 2 (b) and (d)) and after (Fig. 2 (c) and (e)) correction by the adaptive optics are shown in the rest of Fig. 2. Once residual system aberration was corrected, the deformable mirror (DM) was held fixed, and we proceeded with aberration measurements of mouse eyes.

A typical temporal trace of the root mean square (RMS) error of

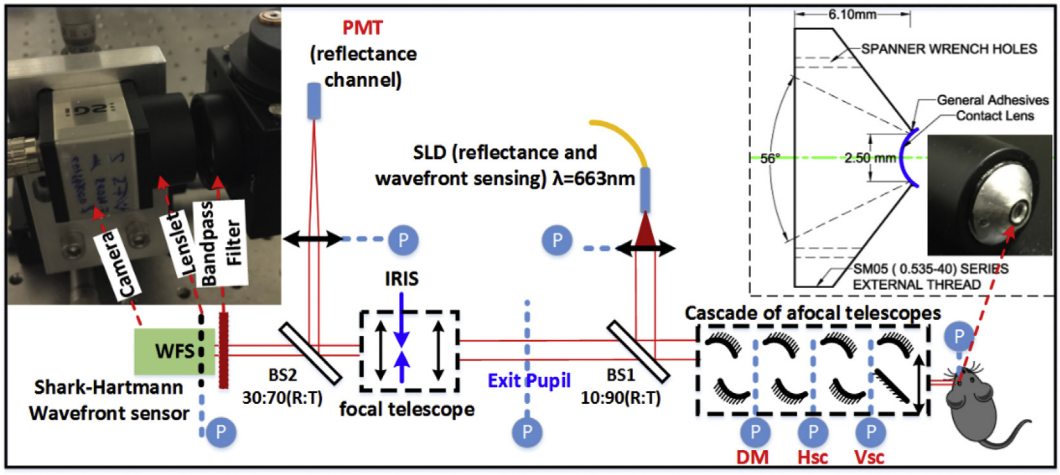

Fig. 1. Schematic of the AO-SLO system. Inset (left): photo of the wavefront sensor; inset (right): design drawing and photo of the contact lens mount prototype. Abbreviations: BS#, beam splitter; DM, deformable mirror; Hsc, horizontal scanner; Vsc, vertical scanner; SLD, superluminescent diode; WFS, wavefront sensor; PMT, photomultiplier tube; R: Reflectance, T: Transmission; P (circled in blue) optical pupil conjugate planes. (For interpretation of the references to colour in this figure legend, the reader is referred to the Web version of this article.)

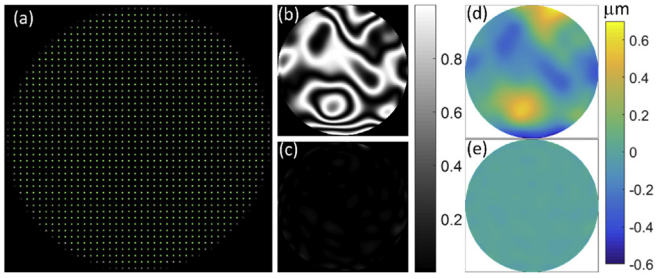

Fig. 2. SHWS spots pattern and system aberration correction. (a) spots pattern from a model eye (green are active spots, 1264 in total); (b), (c) normalized system aberration simulation of fringe map before and after AO correction for the model eye, respectively; (d), (e) system aberration wavefront map before and after AO correction for the model eye, respectively. (For interpretation of the references to colour in this figure legend, the reader is referred to the Web version of this article.)

ocular aberration during AO correction in the living mouse eye is shown in Fig. 3 (a). A full correction is usually completed within 0.25 s, and the correction brings the residual measured RMS aberration below , $\lambda/14$ which is considered diffraction-limited imaging performance according to Maréchal criterion. The fast temporal sampling of the wavefront sensor can track RMS oscillations arising from the frame scanning and mouse's breathing. Once the adaptive optics successfully closed the loop, the photoreceptor mosaic in the mouse retina becomes visible, as shown in Fig. 3 (b). This confirms successful measurement and correction of aberrations in our AO system, as imaging of the mouse rod mosaic, whose average center-to-center spacing is less than 2.0 μm (Geng et al, 2011; Jeon et al., 1998), requires diffraction-limited performance with a 2-mm mouse pupil. Fig. 3(c) shows the angular averaged power spectrum of the photoreceptor mosaic image. The spectrum has a local maximum at 27 cycles/degree corresponding to a center-to-center spacing of 1.60 μm, assuming 43 μm/degree scaling for this image. The specific value of this scaling factor will be discussed in detail in the next section; the scaling factor value of 43 μm/degree was measured experimentally and reported in our previous work describing measurements of rhodopsin bleaching and light-induced increases of fundus reflectance in mice with an SLO employing the same contact lens and type of lens mount. The principal major difference between these two systems for imaging performance is the pupil size, which should not affect the scaling factor (Zhang et al, 2016a).

To study the effect of a contact lens on mouse ocular aberrations, two groups of C57BL/6J (pigmented) mice were examined: young (2.5 months old, n = 10 eyes) and old (14 months old, n = 10 eyes). Pigmented mice were used since the presence of melanin in RPE/choroid is needed for successful wavefront sensing as it provides a well-defined reference plane where light from the imaging beacon get scattered. (We expect that the results of our studies should also apply to the animals with different pigment levels (including albino), but direct measurement of aberrations is not currently possible for non-pigmented ones). During our measurements, mice were anesthetized with the inhalational anesthetic isoflurane (2% in O_2), and pupils dilated with tropicamide and phenylephrine. Ocular aberrations of each eye were measured first without, and then with the contact lens (0 Diopter, 3 mm in diameter, 1.75 mm in radius; Unicon Corporation, Osaka, Japan). When ocular aberrations were measured without a contact lens, no gel was used. Only a small amount of artificial tear drops (i-drop, I-MED Pharma Inc, Canada) were applied after the pupil dilation and then wiped off before the measurement. This helped to maintain the tear film to keep the cornea moist for a short wavefront measurement. When the contact lens was used, a gel (GelTeal Tears, Alcon, U.S.) was placed between the lens and the cornea. The gel was always included when a contact lens was used, and never by itself. As we will describe below, the gel reduces the refractive power of the back surface of the contact lens and the front surface of the cornea relative to their state with tears. All mouse husbandry and handling including imaging was in accordance with animal study protocol approved by the University of California Animal Care and Use Committee (IACUC), which is accredited by Association for Assessment and Accreditation of Laboratory Animal Care (AAALAC) International and strictly adhere to all NIH guidelines.

3. Results

3.1. Effective focal length and the scaling factor of visual angle to μm on the retina

The contact lens used in our experiments has a refractive power of 0 diopters, but its curvature may not perfectly match that of the cornea of every mouse. In addition, the gel layer between the cornea and the contact lens is expected to reduce the refractive power of the back surface of the contact lens and the front surface of the mouse cornea, thereby changing the refractive power of the whole eye. Consistent with these expectations, we observed that the focal plane is shifted axially by varying the gel thickness. Thus, the lens and gel thickness change the nodal point of the compound objective comprising the contact lens, gel and eye's optics. Change in the nodal position necessarily alters the scaling factor relating scanning angle to lateral distance in μm on the retina, a factor important for accurate quantification of the cellular

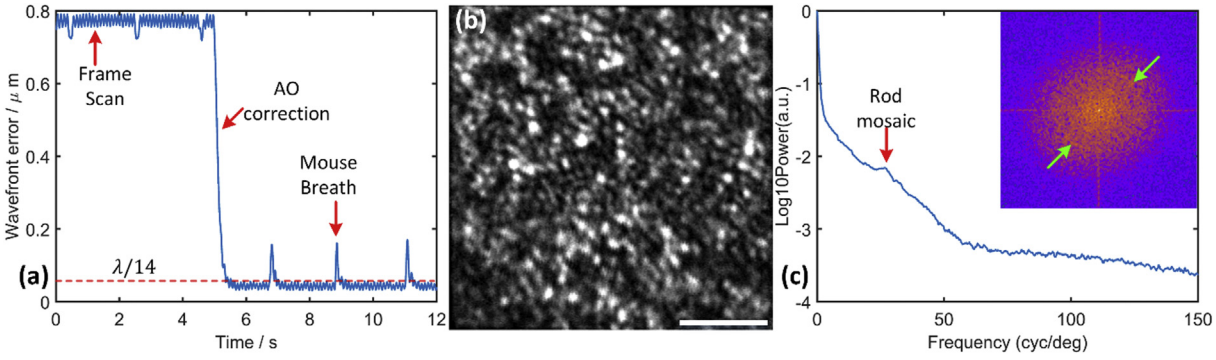

Fig. 3. Performance of our AO system for wavefront aberration correction of mouse eye. (a) Wavefront error changes (dashed red line: diffraction-limited wavefront error); (b) Photoreceptor mosaic image (663 nm reflectance, displayed in a linear 8-bit gray scale that matches the observed dynamic range of photoreceptor reflectivity; scale bar 10 μm); In this experiment the AO system loop was closed without defocus offset to get this image. The exact axial location of the resulting focal plane cannot be determined in our current system.; (c) Angular averaged power spectrum (inset: Fourier power spectrum of the mosaic image, green arrows point to ring-like energy density corresponding to local maximum in power spectrum plot). The local peak at 27 cycles/deg (red arrow) is labeled as "Rod mosaic" whose center-to-center spacing is independently known from histology to be about 1.6 μm (Jeon et al., 1998)); cones comprise only 3% of mouse photoreceptors. (For interpretation of the references to colour in this figure legend, the reader is referred to the Web version of this article.)

Table 1
Key parameters of the Zemax mouse eye model with contact lens and gel.

	Radius (mm)	Thickness (mm)	Refractive Index	Material
Contact lens	1.75	0.250	1.65	
Gel	1.75	0 – 1.70	1.35	Hypromellose 0.3%
Anterior Cornea	1.34	0.105	1.40	
Posterior Cornea	1.30	0.525	1.34	
Anterior Lens	1.00	2.050	1.55	
Posterior Lens	−0.90	0.550	1.34	
Anterior Retina	−1.60	0.220	1.34	
Back of Retina	−1.50			

structure size and the system lateral resolution, and for determining energy density of scanning beams (Zhang et al, 2016a). To investigate these two issues quantitatively a mouse eye model based on G. Bawa et al. (Bawa et al, 2013), was developed with Zemax software (Table 1), and optimized by application of two criteria:

1. The model eye without the contact lens has a 34 μm per visual degree scaling factor, and focuses on the photoreceptor layer for wavefront sensing light (663 nm);
2. With the contact lens and an ~1 mm gel layer the beam focuses on the photoreceptor layer, as observed experimentally.

The model eye of the adult mouse has a scaling factor of 34 μm/deg on the retina (Fig. 4(a)) (Geng et al, 2012). As expected the focal length is shifted by the 0-diopter contact lens combined with gel, and varies systematically with gel thickness (ΔL) (Fig. 4 (b)). A magnified version of the red rectangle in Fig. 4 (b) is shown in Fig. 4 (c). The focus shift (Δz) can be measured by the thickness changes of the vitreous (axial shifting of the retina) so that the focus falls on the back surface of the retina; and the scaling factor can be obtained by tilting the incoming ray by 1° (red ray shown) and measuring the central ray height on the back surface of the retina. The gel thickness was varied from 0 to 1.7 mm at 0.1 mm interval, and the corresponding focus shift (blue curves) and scaling factor (red curves) are shown in Fig. 4 (d). The blue curve shows that the beam focus could be shifted from behind the retina (~200 μm) to the front of the retina (~220 μm) by a 1.7 mm gel layer. When the gel layer is equal to about 0.95 mm, the beam focuses on the photoreceptor layer (the left light blue dashed line), and the corresponding scaling factor is equal to 43 μm/deg (indicated by the right side dashed purple line and star). We emphasize that the scaling factor of 34 μm/degree (horizontal dashed black line and star) is for the natural eye, and that the scaling factor can vary from 35.5 to 51.6 μm/degree, depending on the gel thickness. In practice, since we always optimize focus at the photoreceptor layer by minimizing the defocus terms while aligning the mouse, a 43 μm/deg scaling factor for the mouse with contact lens in our experiments is reasonable. Also, the 1.6 μm center-to-center spacing calculated by this factor matches results obtained *ex vivo* (Jeon et al., 1998). This simulation explains why the scaling factor increases when a contact lens and gel are used for retinal imaging in mice, as previously observed (Zhang et al, 2016a). We also simulated contact lenses with 1.65 mm and 1.55 mm radii of curvature, as shown in the dashed blue and red lines in Fig. 4 (d). The corresponding scaling factors are indicated by the yellow and green stars, respectively. The focal point with a 0-mm thickness gel was shifted closer to the photoreceptor layer from behind the retina by reducing the radius of curvature of the contact lens. Nonetheless, the scaling factor remains larger than that of the natural eye. Overall, use of a contact lens increases the scaling factor.

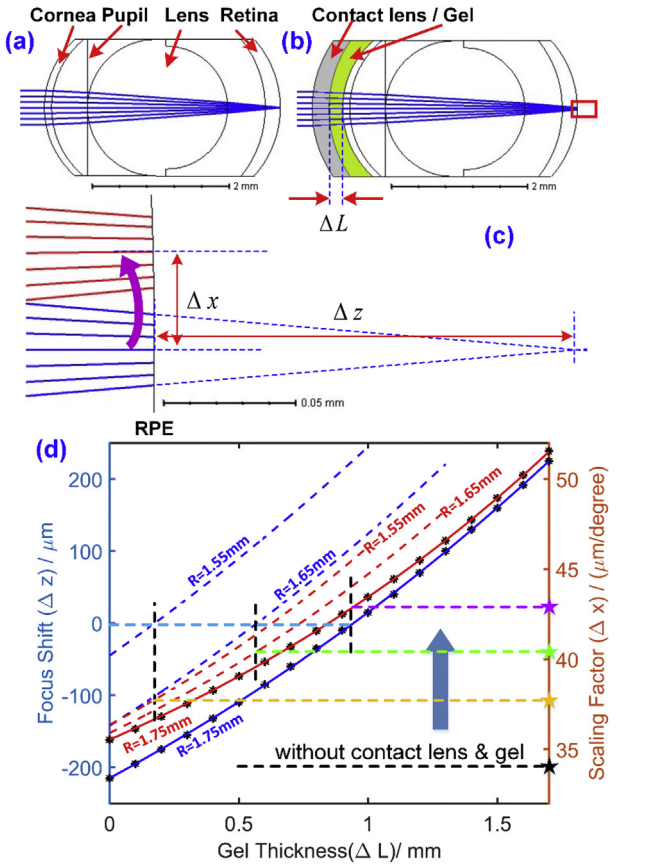

Fig. 4. Zemax modeling of the mouse eye with and without a contact lens. (a), (b) Schematics of the mouse eye with (a), and without (b) the contact lens and gel layer; (c) sketch of focus shift, and of the scaling factor converting visual angle to μm on the retina. (d) The relationship between the focus shift/scaling factor, and the gel thickness for contact lenses with different radii of curvature (R values on plot).

3.2. Wavefront measurement of mouse eye aberrations

The aberrations of the two groups of young and old C57BL/6J mice were measured with, and without contact lenses. In all cases the beam at the pupil was 2.0 mm. The measured wavefronts were fitted with 2 dimensional Zernike polynomials of 66 terms (normalized, up to and including 10th order according to ANSI standards (Thibos et al., 2000)), and the total RMS error calculated by setting piston, *x*-tilt, *y*-tilt, and defocus to zero:

$$E_{rms} = \sqrt{\sum_{i=0}^{N} (Z_i)^2} \quad (1)$$

where $N = 65$, Z_i represents the Zernike coefficients, with Z_0, Z_1, Z_2, $Z_4 = 0$. The total RMS error for the four groups of mice are shown in Fig. 5 (a). Even the best-corrected eye (#2 of the young group) had aberration well above those needed for diffraction-limited performance (RMS ($\lambda/14$) = 0.047 μm, Maréchal criterion).

The averaged aberrations of each group are shown in Fig. 5 (b). The young mouse group has average RMS errors of 0.276 ± 0.070 μm (mean ± SEM (standard error of mean)), and 0.339 ± 0.057 μm, without and with the contact lens, respectively. The old group has average RMS error of 0.436 ± 0.034 μm, and 0.455 ± 0.062 μm, respectively. The old group's average aberrations are ~1.6-fold greater than those of the young group. The contact lens increased the aberration by 4% and 23% for old and young mice, respectively, conflicting with the speculation in our previous study (Zhang et al., 2015a, Zhang et al., 2016b). These results suggest that, similarly to earlier

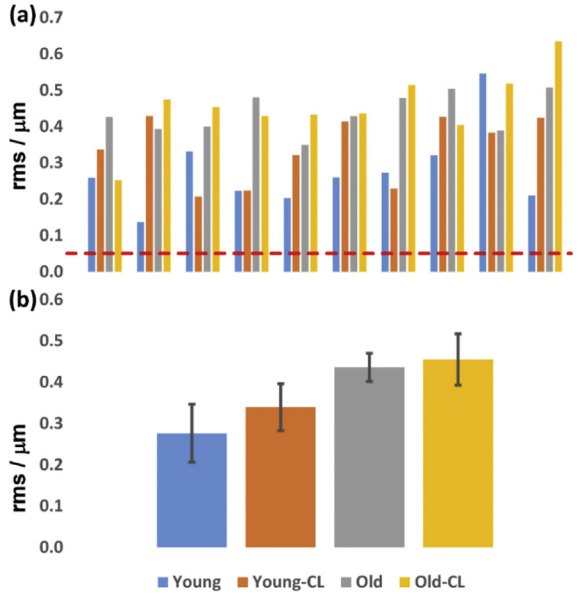

Fig. 5. The mouse eye aberration (total RMS error), measured over 2 mm pupil, comparison between different experimental groups. (a) Abberations of 40 individual mice. Dashed red line: diffraction-limited RMS (λ/14 = 0.047 µm); (b) Averaged aberrations for each group. Abbreviations: Young: 2.5-month-old mice; Old: 14-month-old mice; the suffix "-CL" indicates use of contact lens and gel; absence of suffix indicates that the contact lens and gel were not used. (For interpretation of the references to colour in this figure legend, the reader is referred to the Web version of this article.)

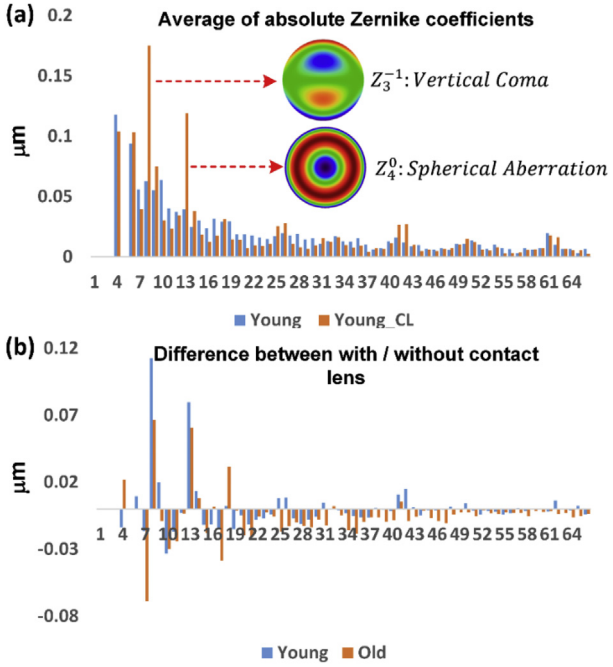

Fig. 6. The Zernike aberrations coefficients decomposition. (a) The averaged absolute Zernike coefficients for the young group of mice with and without the contact lens; (b) The difference of each averaged absolute Zernike terms for young and old mice. Abbreviations: Young: 2.5-month-old mice; Old: 14-month-old mice; the suffix "-CL" indicates use of contact lens and gel; absence of suffix indicates that the contact lens and gel were not used.

observations in humans (Artal et al, 2001). That some of the corneal aberrations might be compensated by the internal optics in the eye. Therefore, correcting corneal aberrations only will not improve overall optical performance of the eye, making the use of Adaptive Optics correction of eye ocular aberrations necessary.

3.3. Zernike decomposition reveals the major refraction error sources introduced by contact lens

To identify the specific sources of the aberrations introduced by the contact lens, we averaged the absolute Zernike coefficients, and compared the Zernike coefficients obtained with and without the contact lens; the results for the young group is shown in Fig. 6 (a). The reason for averaging the absolute Zernike coefficients was to avoid the cancellation between positive and negative Zernike coefficients, to better highlight the major error sources. We identified two major aberrations introduced by the contact lens: the first is vertical coma, and the second is primary spherical aberration. The difference for both young and old groups with and without contact lens is shown in Fig. 6 (b). The contact lens helps to reduce most of the Zernike aberration terms (39 out of 62 terms), while increasing 6 terms for both groups, and staying neutral for other 17 terms. Two of the increased terms - vertical coma and spherical aberration - make major contributions on the total wavefront error. If vertical coma and spherical aberration could be decreased to their level in the absence of a contact lens, then the total RMS errors for the young and old groups with the contact lens would be decreased to 93% and 91% respectively of the errors without the contact lens. This however is still significantly above diffraction-limited wavefront error, suggesting an additional source of aberrations in the internal optics of the eye.

To better understand the sources of the observed spherical and coma aberrations introduced by use of contact lens with gel, we used a Zemax model of an optical system comprising of the front surface of mouse cornea, the contact lens and gel in between (Fig. 7) to investigate how the relative positions of contact lens and cornea (including gel thickness and off axis placing of the contact lens) affect the total aberrations of this system. The aberrations introduced by this model were piston, defocus, and spherical terms (primary, secondary, etc). We omitted higher order spherical terms with coefficients less than 1/10th that of primary spherical aberration, and varied the gel thickness and contact lens curvature changes (Fig. 7 (b)). The model revealed a tradeoff: the smaller the contact lens curvature, the higher the spherical aberration caused by increasing the gel thickness. As expected the spherical aberration came from both the contact lens and gel.

Coma was not present at all in the simulation for an on-axis contact lens, but appeared if the contact lens was shifted off-center. We simulated vertical coma by shifting the contact lens up and down. This direction of displacement is more difficult to control than horizontal shifting in our optical system, hence a potential source of coma. Currently a heavy-duty lab jack (L490, Thorlabs, US) with manually adjustable position knob was used to control the vertical displacement; this positioner has a non-linear displacement per turn and is not as accurate as the horizontal positioner, which is controlled by Vernier micrometer. (In the future, the lab jack will be replaced with a linear micrometer driven stage to provide more precise control over the vertical positioning). The model analysis shows that displacement of a contact lens by as little as ~30 µm is sufficient to increase the amplitude of vertical coma measured in our study. The simulation (Fig. 7 (c)) reveals that coma is less sensitive to gel thickness than to changes in the radius of curvature: thus, the slopes of the black solid and dashed curves for which the gel thickness differs by a 0.6 mm differ by less than those obtained by changing the radius of curvature with 0.1 mm (red and blue curves).

3.4. Pupil size effect on aberrations

To extend our studies to the smaller pupil sizes used in non-AO mouse retinal imaging systems, we calculated the wavefront aberration for different pupil sizes, by apodizing the pupil, and re-analyzing the

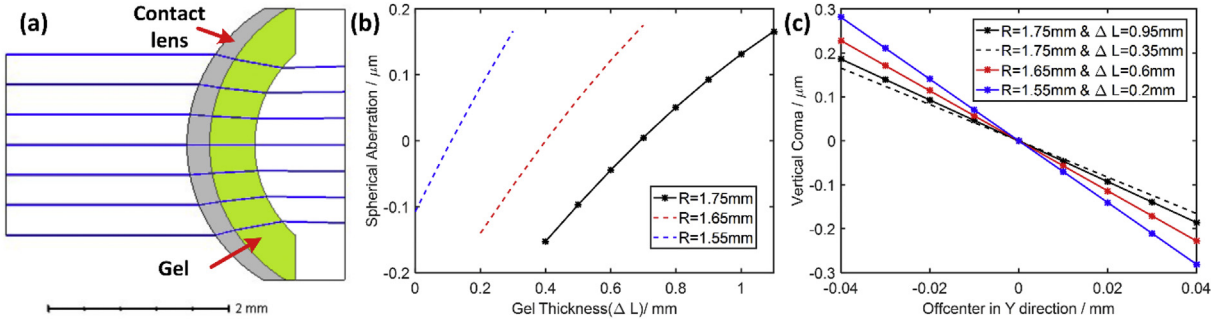

Fig. 7. Trace the aberration error sources introduced by usage of contact lens and gel. (a) Simplified Model; (b) Spherical aberration related to gel thickness and contact lens curvature (R); (c) Coma related to off-center shift, gel thickness (ΔL) and contact lens curvature (R). The three solid line curves were obtained using optimal gel thicknesses (ΔL) as determined in Fig. 4 (d).

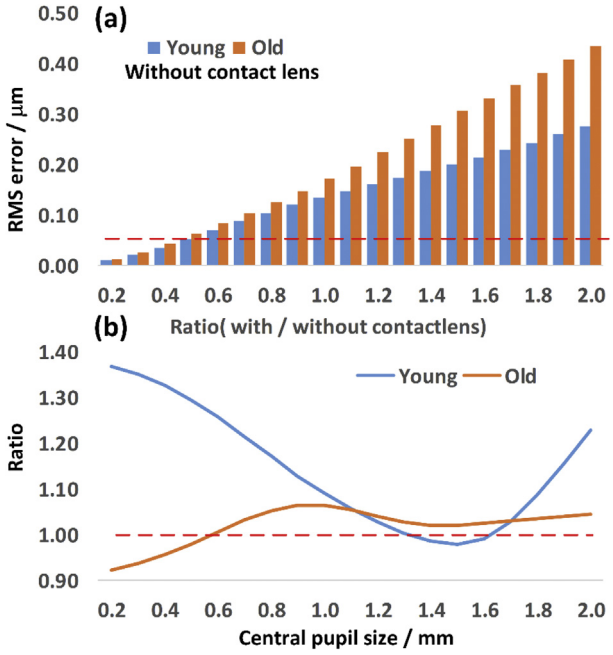

Fig. 8. Comparison across different central pupil size: (a) the total RMS error from young (2.5 months) and old (14 months) group mice without contact lens; Red dashed line highlights the diffraction-limited RMS. (b) the ratio of total RMS error with and without the contact lens. Red dashed line highlights the line corresponding to ratio = 1. (For interpretation of the references to colour in this figure legend, the reader is referred to the Web version of this article.)

aberrations after apodization with normalized Zernike terms. Then, we calculated the wavefront RMS error using Eq (1). after setting tip, tilt and defocus terms to zero. Results comparing average of young and 'old' mice without contact lens are shown in Fig. 8 (a). There is less difference in aberration between the two groups when the pupil is smaller than 0.8 mm: aberration is about 1.2-fold times greater for old than young, a difference that is smaller than the 1.6-fold difference between two groups with full-pupil. In addition, we demonstrated the contact lens effect by calculating the ratio of the RMS wavefront error between the cases with and without contact lens for both young and old groups: the result is shown in Fig. 8 (b). Interestingly, for this group of old mice, the contact lens reduces aberration when the pupil is smaller than 0.6 mm (Ratio < 1). For the young group of mice, the contact lens also helps to slightly reduce overall aberration, when the pupil was within the range of 1.3–1.6 mm.

3.5. Lateral resolution and Strehl Ratio changes along with the input beam size at mouse pupil

Our aberration measurements also serve to provide general guidelines for non-AO mouse retinal imaging systems. For the previously described widefield SLO system (Zhang et al, 2015b), which uses a single mode fiber to deliver excitation light (490 nm) and a large detection pinhole (multimode fiber) to collect emitted light (530 nm), its performance (full-width at half-maximum, FWHM, of retinal focus) with different input beam sizes at the mouse pupil can be assessed by computing its lateral resolution $\overline{FWHM}_D$ given by the averaged PSF diameter (Zhang et al, 2015b):

$$\begin{cases} PSF & = P_{input} \cdot P_{output} \\ & = (P_{ls} \otimes (M_{ls} \cdot S_{ls})) \cdot (P_{det} \otimes (M_{det} \cdot S_{det})) \\ \overline{FWHM}_D & = 2 \cdot \sqrt{A_{PSF}/\pi} \end{cases} \quad (2)$$

where P_{ls} and P_{det} are the point-spread functions (*PSF*) determined by the light source (*ls*) and detection (*det*) numerical apertures, M_{ls} and M_{det} are the magnification factors between the conjugate image planes (the mouse retina and the light source/detection fiber tips), S_{ls} and S_{det} are the core size of the light source and detection fibers, respectively, and A_{PSF} is the area enclosing *PSF* intensities above its half-maximum, and the symbol ⊗ indicates 2D convolution. (Eq. (2) reduces to the conventional definition when the PSF is radially symmetric). The lateral resolution for different input beam sizes is shown in Fig. 9 (a): the contact lens reduces resolution more for the young mice. Overall the results show that the lateral resolution improves with increasing pupil size for all mice. One could expect higher resolution by moderately increasing the mouse pupil used for imaging for all the mice. Also, since a relatively large pinhole (multi-mode fiber with 50 μm core size) was used in our system, the overall (dual-pass) PSF will be largely dependent on the input/excitation PSF, because it is much smaller than the output/detection PSF, as shown in Fig. 9 (b) black and blue solid lines, respectively. By using equal configuration (single mode fiber and same collimating lens) in both light source and detection end, a better PSF resolution could be expected, as shown in Fig. 9 (b) solid and dashed red lines, respectively.

We calculated the Strehl Ratio (SR) according to ref (Roberts et al., 2004) as

$$S = \frac{I(x=0)}{P(x=0)} \quad (3)$$

where, x is the position vector, $I(x = 0)$ is the maximum of the PSF with aberration, and $P(x = 0)$ is the maximum of the diffraction limited PSF. Fig. 9 (c) shows the contact lens decrease the SR for young mice while increase the SR for old group mice. Overall the averaged SR for all groups dramatically decrease along with the input beam size increasing. This represent reduction of sensitivity of the instrument to measure retina structures. We also calculated the averaged input and output

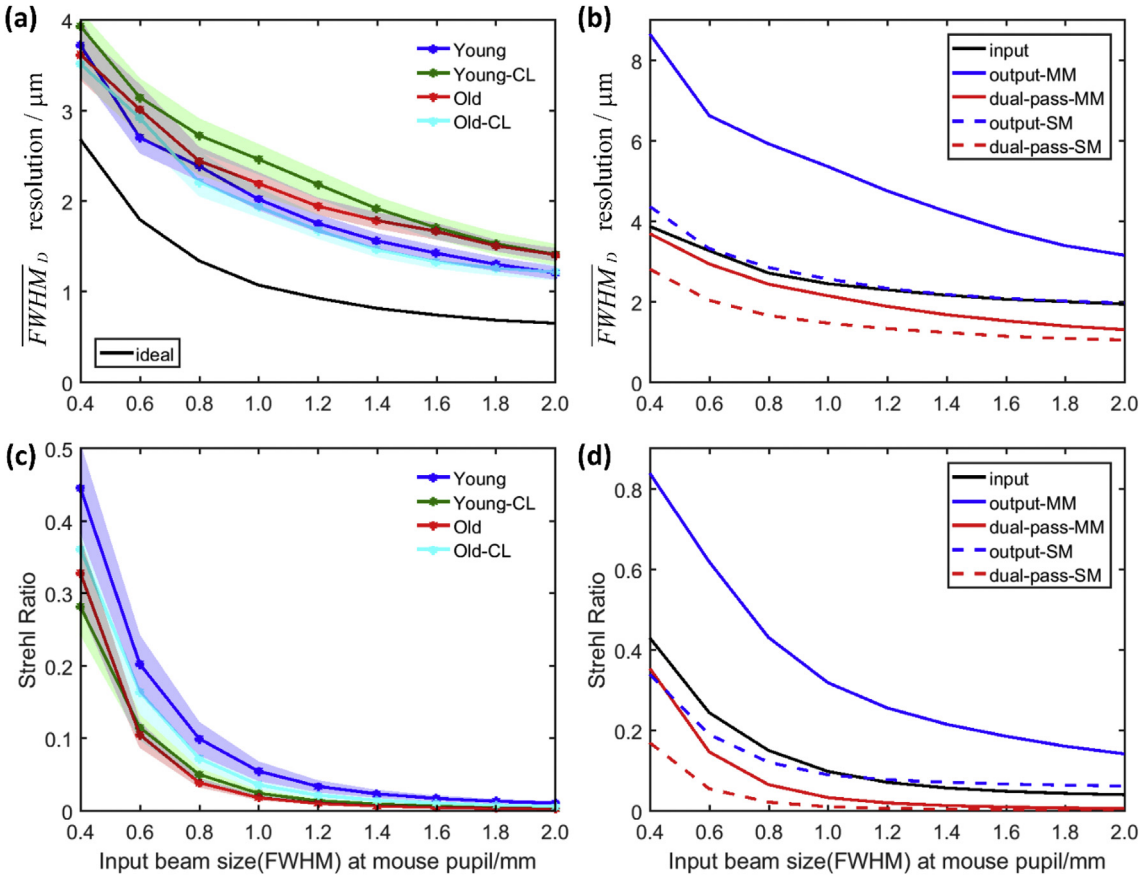

Fig. 9. Simulated effects of illumination beam size at mouse pupil for (a) $\overline{FWHM}_D$ resolution for different group mice with multi-mode (MM) fiber detection (b) averaged input/output/dual-pass $\overline{FWHM}_D$ for detection with MM/single-mode (SM) fiber, (c) Strehl Ratio (SR) for different group mice with MM fiber detection (d) averaged input/output/dual-pass SR for detection with MM/SM fiber; (a), (c) Each data point is the average of data from 10 eyes, and is plotted as mean ± SEM (standard error of mean); (b), (d), each line was averaged from all 40 eyes. (Note that the results in (a) and (c) have a different sequence with the overall RMS error showing in Fig. 5(b)).

Strehl Ratio for both detections: with multi-mode or single mode fibers. Again, the SR is largely dependent on the SR of P_{input} for detection with the large pinhole of the multimode fiber: if the detection aperture is instead a single mode fiber whose size is close to the diffraction-limited Airy disc, the SR of the collection P_{output} will be much smaller, as shown in Fig. 9 (d). However, this will necessarily further reduce the system's sensitivity.

4. Discussion and conclusion

Reliable measurements of mouse retinal structure and function *in vivo* require understanding and control of as many as possible of the optical and physiological variables that can affect image quality and tissue function (Zhang et al, 2017; Zhang et al, 2016a). One clear requirement for imaging in lengthy sessions necessary to assess many physiological features of the eye is maintenance of the optical quality and transparency of the cornea throughout the session. This can be only achieved by covering the cornea with a microscope cover slip, contact lens or specialized objective, along with a medium that help maintains natural hydration. Such strategies can degrade optical performance and quantitatively alter light delivery if the optical properties of the additional elements are not accurately understood or controlled. In this manuscript we used our ability to monitor ocular aberrations in the mouse eye *in vivo* with an adaptive optic system to obtain insight into the optical performance of commercially available mouse hard contact lenses. We anticipate that this analysis will help in improving the design and application of contact lenses in mouse retinal imaging.

In the introduction, two approaches to use of a contact lens (putting on the cornea directly or attaching to the mount) were described. The first approach can be an extreme case of the second one, thus the expectations for a gel thickness of zero can be extrapolated from our results: there is still spherical aberration for the contact lens placed directly on the eye. Ideally, the spherical aberration should be compared between the contact lens and eye combination versus the eye alone. However, the model eye used in this study has spherical aberration much higher than the measured data. Since the aberrations measured here with and without a contact lens directly reflect the properties of the optical system of the mouse eye, the Zemax model we implemented is not fully faithful to this feature of the mouse eye and improved models need to be developed in the future. For example, the mouse lens in our model doesn't have a gradient index (Goncharov and Dainty, 2007; Campbell and Hughes, 1981), and this could be one of the reasons that our mouse eye model has higher spherical aberration than the measured data. Nonetheless, the model eye enables the effects of variation of specific optical parameters, including the lens curvature and gel thickness, to be explored in a manner that provides insight into these effects. Ongoing development of an improved mouse model eye is underway.

The gap between the contact lens and cornea is filled with gel, which permits focus shifting onto different retinal layers, but also contributes to spherical aberration and misalignment. A separate mechanism for focus shifting could be considered. Our study shows that vertical coma is one major aberration source, but it is due to misalignment. This suggests a problem with the mouse alignment methodology, not the use of a contact lens. An additional method could include use of OCT to visualize the fit of a selected contact lens to the

mouse eye to record the decentering, tilt, etc (Jian et al., 2013). This would help with alignment of the mouse to fit the contact lens better.

In conclusion, if not maintained in a hydrated state, the optics of the anesthetized mouse eye can undergo changes during an imaging session that seriously compromise the quality of images collected with different retinal imaging modalities. The use of a contact lens with a water-retaining gel greatly stabilizes the eye's optics, enabling imaging sessions of up to several hours. However, a contact lens also introduces static changes in the optics, including increasing the effective focal length of the eye and thereby the scaling factor between visual angle and distance μm (on the retina), which is needed for a full characterization of the sizes of retinal features such as the photoreceptor mosaic (Fig. 3). The effect of a contact lens and gel on ocular aberration is complex. In our system, the use of a contact lens introduced vertical coma and spherical aberrations above those of the native eye. Our analysis suggested that vertical coma was caused by inadequate alignment of the contact lens axis with the optical axis of the eye, which could be corrected by a use of higher precision vertical displacement stage. Additional improvement in image quality could be achieved by choice of the contact lenses with curvatures that better match specific groups of mice (Childs et al, 2016), or by adopting a soft contact lens with flexible curvature to better match the mouse cornea, or use of more advanced contact lenses (correcting spherical aberrations).

Although both wavefront sensor-based AO- (Geng et al, 2012; Zawadzki et al, 2015), and wavefront sensorless AO-systems (Bonora et al, 2015; Wahl et al, 2016; Jian et al, 2014) are used to correct ocular aberrations in order to achieve diffraction limited performance, the specific requirements of the wavefront corrector and deformable mirror (DM) (stroke and number of actuators), depend on the actual aberrations that need to be corrected. Our aberration measurements should be useful for further assessment of the performance of a given deformable mirror for mouse retinal imaging with AO. Also, for computational AO method (Adie et al, 2012; Shemonski et al, 2015) applied to mouse, it should also be helpful in correcting the major static error sources and maintaining them at a relatively low level.

Acknowledgments

Authors would like to acknowledge their funding sources: NSF I/UCRC CBSS Grant, NIH grants EY02660, EY026556, and EY012576 (NEI Core Grant). We thank Dr. Marie Burns and Dr. John S. Werner for help and support.

Appendix A. Supplementary data

Supplementary data related to this article can be found at http://dx.doi.org/10.1016/j.exer.2018.03.027.

References

Adie, S.G., et al., 2012. Computational adaptive optics for broadband optical interferometric tomography of biological tissue. In: Proceedings of the National Academy of Sciences of the United States of America. vol. 109. pp. 7175–7180 19.
Artal, P., et al., 2001. Compensation of corneal aberrations by the internal optics in the human eye. J. Vis. 1 (1).
Bawa, G., et al., 2013. Variational analysis of the mouse and rat eye optical parameters. Biomed. Optic Express 4 (11), 2585–2595.
Bermudez, M.A., et al., 2011. Time course of cold cataract development in anesthetized mice. Curr. Eye Res. 36 (3), 278–284.
Biss, D.P., et al., 2007. In vivo fluorescent imaging of the mouse retina using adaptive optics. Optic Lett. 32 (6), 659–661.
Bonora, S., et al., 2015. Wavefront correction and high-resolution in vivo OCT imaging with an objective integrated multi-actuator adaptive lens. Optic Express 23 (17), 21931–21941.
Campbell, M.C.W., Hughes, A., 1981. An analytic, gradient index schematic lens and eye for the rat which predicts aberrations for finite pupils. Vis. Res. 21 (7), 1129–1148.
Castejón-Mochón, J.F., et al., 2002. Ocular wave-front aberration statistics in a normal young population. Vis. Res. 42 (13), 1611–1617.
Childs, A., et al., 2016. Fabricating customized hydrogel contact lens. Sci. Rep. 6.
Clemens, Alt, et al., 2012. In Vivo Tracking of Hematopoietic Cells in the Retina of Chimeric Mice with a Scanning Laser Ophthalmoscope. IntraVital.
Fischer, M.D., et al., 2009. Noninvasive, in vivo assessment of mouse retinal structure using optical coherence tomography. PLoS One 4 (10), e7507.
Fuerst, P.G., et al., 2008. Neurite arborization and mosaic spacing in the mouse retina require DSCAM. Nature 451 (7177), 470.
Geng, Y., et al., 2011. Optical properties of the mouse eye. Biomed. Optic Express 2 (4), 717–738.
Geng, Y., et al., 2012. Adaptive optics retinal imaging in the living mouse eye. Biomed. Optic Express 3 (4), 715–734.
Goncharov, A.V., Dainty, C., 2007. Wide-field schematic eye models with gradient-index lens. Journal of the Optical Society of America a-Optics Image Science and Vision 24 (8), 2157–2174.
Guevara-Torres, A., Williams, D.R., Schallek, J.B., 2015. Imaging translucent cell bodies in the living mouse retina without contrast agents. Biomed. Optic Express 6 (6), 2106–2119.
Helmstaedter, M., et al., 2013. Connectomic reconstruction of the inner plexiform layer in the mouse retina. Nature 500 (7461), 168.
Huang, D., et al., 1991. Optical coherence tomography. Science (New York, NY) 254 (5035), 1178.
Jeon, C.J., Strettoi, E., Masland, R.H., 1998. The major cell populations of the mouse retina. J. Neurosci. 18 (21), 8936–8946.
Jian, Y.F., Zawadzki, R.J., Sarunic, M.V., 2013. Adaptive optics optical coherence tomography for in vivo mouse retinal imaging. J. Biomed. Optic. 18 (5).
Jian, Y.F., et al., 2014. Wavefront sensorless adaptive optics optical coherence tomography for in vivo retinal imaging in mice. Biomed. Optic Express 5 (2), 547–559.
Jiang, H., et al., 1996. Phospholipase C β4 is involved in modulating the visual response in mice. Proceedings of the National Academy of Sciences 93 (25), 14598–14601.
Liu, X., et al., 2013. Effect of contact lens on optical coherence tomography imaging of rodent retina. Curr. Eye Res. 38 (12), 1235–1240.
Mocci, J., et al., 2018. A multi-platform CPU-based architecture for cost-effective adaptive optics systems. IEEE Transactions on Industrial Informatics PP 99 (1–1).
Paques, M., et al., 2006. High resolution fundus imaging by confocal scanning laser ophthalmoscopy in the mouse. Vis. Res. 46 (8–9), 1336–1345.
Porter, J., et al., 2001. Monochromatic aberrations of the human eye in a large population. JOSA A 18 (8), 1793–1803.
Roberts, L.C., et al., 2004. Is that really your Strehl ratio? In: Calia, D.B., Ellerbroek, B.L., Ragazzoni, R. (Eds.), Proceedings of the Society of Photo-optical Instrumentation Engineers (Spie). Advancements in Adaptive Optics, pp. 504–515 Pts. 1–3.
Seeliger, M.W., et al., 2005. In vivo confocal imaging of the retina in animal models using scanning laser ophthalmoscopy. Vis. Res. 45 (28), 3512–3519.
Shemonski, N.D., et al., 2015. Computational high-resolution optical imaging of the living human retina. Nat. Photon. 9 (7), 440–U477.
Srinivasan, V.J., et al., 2006. Noninvasive volumetric imaging and morphometry of the rodent retina with high-speed, ultrahigh-resolution optical coherence tomography. Invest. Ophthalmol. Vis. Sci. 47 (12), 5522–5528.
Thibos, L., et al., 2000. Standards for reporting the optical aberrations of eyes. In: OSA Technical Digest, Vision Science and its Applications SuC1.
Thibos, L.N., et al., 2002. Statistical variation of aberration structure and image quality in a normal population of healthy eyes. JOSA A 19 (12), 2329–2348.
Wahl, D.J., et al., 2016. Wavefront sensorless adaptive optics fluorescence biomicroscope for in vivo retinal imaging in mice. Biomed. Optic Express 7 (1), 1–12.
Webb, R.H., Hughes, G.W., 1981. Scanning laser ophthalmoscope. IEEE Trans. Biomed. Eng. 28 (7), 488–492.
Zawadzki, R.J., et al., 2015. Adaptive-optics SLO imaging combined with widefield OCT and SLO enables precise 3D localization of fluorescent cells in the mouse retina. Biomed. Optic Express 6 (6), 2191–2210.
Zhang, P.F., et al., 2015a. In vivo wide-field multispectral scanning laser ophthalmoscopy-optical coherence tomography mouse retinal imager: longitudinal imaging of ganglion cells, microglia, and Muller glia, and mapping of the mouse retinal and choroidal vasculature. J. Biomed. Optic. 20 (12).
Zhang, P.F., et al., 2015b. Effect of scanning beam size on the lateral resolution of mouse retinal imaging with SLO. Optic Lett. 40 (24), 5830–5833.
Zhang, P., et al., 2016a. The photosensitivity of rhodopsin bleaching and light-induced increases of fundus reflectance in mice measured in vivo with scanning laser OphthalmoscopySLO measurement of mouse rhodopsin. Invest. Ophthalmol. Vis. Sci. 57 (8), 3650–3664.
Zhang, Pengfei, et al., 2016b. Fluorescent scanning laser ophthalmoscopy for cellular resolution in vivo mouse retinal imaging: benefits and drawbacks of implementing adaptive optics. SPIE BiOS 96930E–96930E.
Zhang, P., et al., 2017. In vivo optophysiology reveals that G-protein activation triggers osmotic swelling and increased light scattering of rod photoreceptors. Proceedings of the National Academy of Sciences 114 (14), E2937–E2946.